Optics Letters

Hybrid silicon-chalcogenide glass-integrated photonic platform for EDFA-free four-wave mixing

Kunhao Lei,[1,†] Boshu Sun,[2,3,†] Kangjian Bao,[2,3,†] Bo Tang,[4] Yiheng Tang,[2,3] Haojie Zhu,[2,3] Jialing Jian,[2,3] Chunlei Sun,[2,3] William Shieh,[2,3,5] Hongtao Lin,[1,6] and Lan Li[2,3,5,*]

[1]The State Key Lab of Brain-Machine Intelligence, Key Laboratory of Micro-Nano Electronics and Smart System of Zhejiang Province, College of Information Science and Electronic Engineering, Zhejiang University, Hangzhou 310027, China
[2]Zhejiang Key Laboratory of 3D Micro/Nano Fabrication and Characterization, Department of Electronic and Information Engineering, School of Engineering, Westlake University, Hangzhou 310030, China
[3]Institute of Advanced Technology, Westlake Institute for Advanced Study, Hangzhou, Zhejiang 310024, China
[4]Institute of Microelectronics of the Chinese Academy of Sciences, Beijing 100029, China
[5]Westlake Institute for Optoelectronics, Fuyang, Hangzhou, Zhejiang 311421, China
[6]hometown@zju.deu.cn
[†]These authors contributed equally.
*lilan@westlake.edu.cn

Received 18 May 2025; revised 21 July 2025; accepted 28 July 2025; posted 29 July 2025; published 27 August 2025

Here, we demonstrate a nonlinear-integrated photonic platform that integrates $Ge_{28}Sb_{12}Se_{60}$ chalcogenide waveguides with multi-project wafer (MPW) silicon waveguides, enabling an efficient four-wave mixing (FWM) nonlinear parametric process. The nondegenerate FWM nonlinear power threshold of the hybrid-integrated photonic platform is as low as 0.16 mW. By synergistically leveraging the advantages of both optical materials, this work offers a promising avenue for the development of large-scale integrated nonlinear photonic platforms.

https://doi.org/10.1364/OL.568100

As a third-order Kerr nonlinear effect, four-wave mixing (FWM) is a parametric process that enables efficient nonlinear wavelength conversion, with extensive applications in high-precision metrology systems [1], quantum photonics [2], and sensing technologies [3]. Silicon photonic platforms have garnered extensive attention and investigation in nonlinear photonics due to their exceptional compatibility with standard CMOS processes and the significantly large nonlinear refractive index (n_2). However, owing to the significant two-photon absorption (TPA) of silicon within the C-band of optical communication, achieving a low power threshold for FWM becomes challenging [4]. Meanwhile, annealed silicon nitride waveguides, which exhibit ultra-low propagation losses, have been widely demonstrated in frequency comb and octave-spanning supercontinuum processes [5]. Nevertheless, their inherently low nonlinear coefficients still require high pump power (100 mW) for efficient nonlinear parametric processes [6]. Consequently, to realize large-scale CMOS fabrication process-compatible nonlinear photonic-integrated circuits, novel nonlinear photonic materials and back-end-of-line processes must be introduced to promote and realize efficient nonlinear systems with hybrid integration with silicon photonic platforms.

Chalcogenide glass is an amorphous compound primarily composed of chalcogens, such as sulfur (S), selenium (Se), tellurium (Te) (elements from Group VI), and other elements with low electronegativity. Due to its high nonlinear coefficient and minimal TPA effect, chalcogenide glass is regarded as a promising nonlinear photonic material with significant development potential [7]. Moreover, leveraging its amorphous phase characteristics, chalcogenide glass can be directly deposited onto both crystalline and amorphous substrates via low-cost, low-temperature evaporation technology. Therefore, the silicon-chalcogenide glass hybrid integration photonic platform serves as an ideal substrate for on-chip FWM [8]. Simultaneously, numerous research studies have emerged focusing on the hybrid integration of chalcogenide glass with other functional photonic platforms. By leveraging the excellent mechanical properties and high nonlinear coefficient of chalcogenide glass, this integration enables the development of hybrid acoustic-optic modulators [9], waveguide amplifiers [10], frequency converters [11], and other advanced devices [12]. However, achieving large-scale on-chip integration via CMOS-compatible processes remains challenging for these hybrid integration technologies.

This work aims to achieve highly efficient hybrid integration of chalcogenide glass with standardized silicon photonic platforms through back-end-of-line techniques. By leveraging the multi-project wafer (MPW) process along with the back-end-of-line processing technology, we successfully fabricated a GSSe micro-ring resonator (MRR) with a quality factor surpassing 9.8×10^4 and demonstrated the efficient EDFA (erbium-doped fiber amplifier)-free nondegenerate four-wave mixing nonlinear parametric process with a power threshold below zero dBm through the hybrid-integrated photonic platform. This

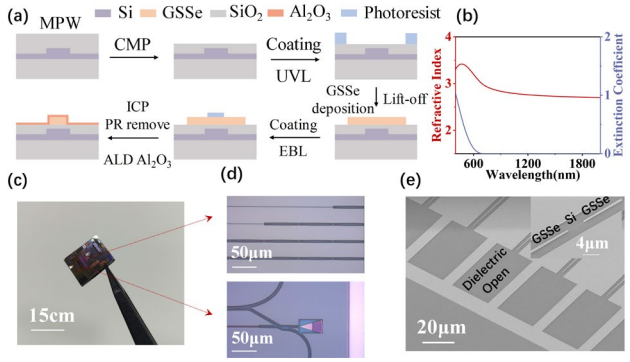

Fig. 1. (a) Flow chart of the back-end-of-line process based on the MPW wafer. (b) Real and imaginary components of the refractive index (n and k) for GSSe thin films. (c) Realistic image of the hybrid-integrated nonlinear photonic chip. (d) Microscopic images of the interlayer couplers and hybrid-integrated MRRs. (e) SEM images of the interlayer coupler (inset: interlayer coupling of the taper waveguide).

technological approach integrates large-scale, low-cost integration benefits of silicon photonics with the exceptional processability and high nonlinear coefficient of chalcogenide glass, thereby providing a promising avenue for expanding the applications of nonlinear silicon photonic platforms.

Silicon photonic devices for hybrid integration were fabricated via a 180-nm node MPW run at the Institute of Microelectronics, Chinese Academy of Sciences (IMECAS). The back-end-of-line workflow for the hybrid integration of MPW-based silicon photonic chips is illustrated in Fig. 1(a). First, the silicon oxide cladding on the top of the MPW silicon photonic chip was reduced to 150 nm through chemical mechanical polishing (CMP). Subsequently, the 500-nm GSSe film was deposited onto the MPW chip via a combination of ultraviolet lithography (UVL), thermal evaporation, and lift-off processes. The refractive index of the GSSe film was determined to be 2.72 at 1550 nm within the communication band using an ellipsometer, as shown in Fig. 1(b). Furthermore, the chip was coated with ARP6200.13 electron beam lithography (EBL) resists and patterned by EBL to define the GSSe waveguide. The waveguide pattern was transferred to the GSSe layer through inductively coupled plasma (ICP) dry etching with CHF_3/Ar gas chemistries. The residual resist on top of the waveguide was removed using oxygen plasma, and the side wall oxidation byproducts can be effectively removed by the hydrofluoric acid solution. Finally, atomic layer deposition (ALD) was employed to coat a 5-nm Al_2O_3 protective layer on the silicon-chalcogenide glass hybrid-integrated photonic chip. Figures 1(c) and 1(d) present realistic images of the Si-GSSe hybrid-integrated photonic chip fabricated by MPW and back-end-of-line processes and detailed microscopic views of the interlayer coupler and MRR, respectively. Figure 1(e) shows the scanning electron microscopy (SEM) image of the grating coupler region for the cascaded interlayer coupler. Signal transmission between the fiber and the silicon grating coupler is achieved by creating the dielectric open window in the GSSe layer on the top. The input propagating through the silicon waveguide couples into the GSSe waveguide located in the upper silicon oxide layer via the interlayer coupler, as illustrated in the inset of Fig. 1(e).

In response to the high-performance MRR requirements for on-chip efficient FWM, we have designed the racetrack MRR

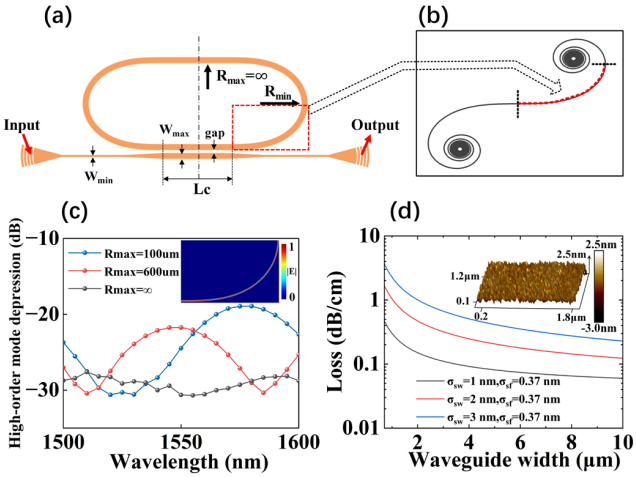

Fig. 2. (a) Structure diagram of the Euler MRR. (b) Schematic diagram of the Euler helical curve. (c) FDTD simulation of Euler MRR high-order mode depression with different R_{max}. (d) The relationship between scattering loss and waveguide width based on the n-w model at a wavelength of 1550 nm (σ_{sw} = 1, 2, and 3 nm, respectively, σ_{sf} = 0.37 nm, inset: atomic force microscopy (AFM) characterization of the surface morphology).

based on the Euler helical structure, as illustrated in Figs. 2(a) and 2(b). The input light propagates from the single-mode waveguide with a width of W_{min} to a multi-mode waveguide with a width of W_{max} via a taper waveguide and subsequently couples into the MRR. The MRR consists of two straight waveguides and four 90-degree curved Euler waveguides [13]. The curvature transitions gradually from the minimum bending radius to an effectively infinite bending radius, where the latter is connected to the straight waveguide. As demonstrated in the FDTD simulation results presented in Fig. 2(c), setting the maximum bending radius to infinity effectively eliminates mode mismatch and suppresses the cumulative transmission of all high-order modes to approximately −30 dB. To predict the scattering loss induced by the roughness, we performed calculations using the n-w model [14]. As shown in Fig. 2(d), the relationship between TE_0 mode scattering loss and waveguide width is presented. Here, the scattering loss is influenced jointly by the side wall roughness and the surface roughness of the waveguide. The standard deviation σ_{sw} of the side wall roughness was set to 1, 2, and 3 nm, respectively, while σ_{sf} represents the surface roughness, which was characterized by AFM with a value of 0.37 nm. It can be observed from the results that a wider waveguide is associated with lower scattering loss and also alleviates the demands on high-precision fabrication processes.

To monitor and optimize the micro-nano fabrication process parameters of the GSSe waveguide, we characterized the performance of single-layer GSSe MRRs and verified the phenomenon of the nonlinear FWM effect in the GSSe MRRs. Specifically, the 500-nm GSSe thin film was deposited on a silicon substrate with a 2-μm thermal oxide layer. The waveguide width of the MRR was set to 1.5 μm to minimize the optical mode's perturbation caused by waveguide sidewall roughness. First, the transmission spectra of GSSe MRR were characterized using tunable lasers, as illustrated in Fig. 3. The MRR exhibited an almost uniformly spaced free spectral range (FSR) of

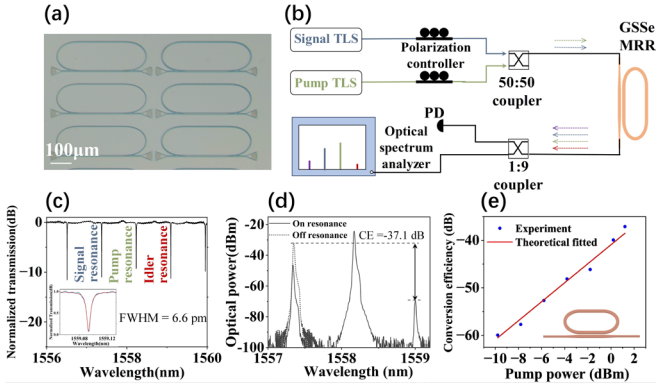

Fig. 3. (a) Microscopic images of the GSSe MRRs. (b) Schematic of the FWM measurement setup (TLSs: Santec TSL-550 TSL-570; OSA: Yokogawa-AQ6730D). (c) Measured transmission spectrum of the GSSe MRR (inset: Lorentz fitting for the resonance peak). (d) Measured output spectra of the GSSe MRR by OSA when the signal is off- and on-resonance. (e) Measured FWM conversion efficiency of the GSSe MRR as a function of the pump power.

approximately 0.86 nm, which corresponds to a calculated group refractive index ng of 2.83. According to Lorentz fitting, the full width at half maximum (FWHM) of the resonant peak at 1559.09 nm is 6.6 pm, resulting in a loaded quality factor (Q_l) of 2.36×10^5. The corresponding intrinsic quality factor (Q_i) was evaluated at 3.71×10^5, indicating a waveguide propagation loss of 1.33 dB/cm.

Furthermore, the FWM nonlinear parameter process of the MRR was characterized and experimentally verified. The schematic diagram of the experimental setup is illustrated in Fig. 3(b). In this study, two tunable laser sources serve as the signal and pump light inputs. The signal and pump lights pass through polarization controllers to ensure the input state remains in TE mode. The signals are combined using a 3-dB coupler before being introduced into the GSSe MRR under test. The output mixing signal from the MRR is split into a 1:9 ratio, with 10% of the energy directed to a photodetector (PD) for intensity measurement and 90% directed to an optical spectrum analyzer for observing the FWM phenomenon. Figure 3(d) illustrates the GSSe MRR's output spectrum under conditions where the signal light is off-resonance and both the signal and pump light are on-resonance. By injecting a 1.32-mW pump light and a 0.01-mW signal light into the MRR while both input lights are simultaneously on resonance, the FWM effect was successfully achieved, resulting in an idle conversion efficiency of −37.1 dB. Further, we investigated the variation of conversion efficiency as a function of pump optical power, as illustrated in Fig. 3(e). The results indicate that GSSe MRR exhibits a low FWM nonlinear power threshold of −9.8 dBm (approximately 0.1 mW). This result also suggests that the MRR and bus waveguide maintain stable coupling across varying pump optical powers with negligible nonlinear loss since the quadratic relationship between conversion efficiency and pump optical power. The conversion efficiency of FWM in MRR can be calculated using the following expression [15,16], which takes into account the key parameters influencing the process:

$$\eta = \frac{P_{i,out}}{P_{s,in}} = \left(\gamma P_p L_{eff}\right)^2 F_p^4 F_s^2 F_i^2, \tag{1}$$

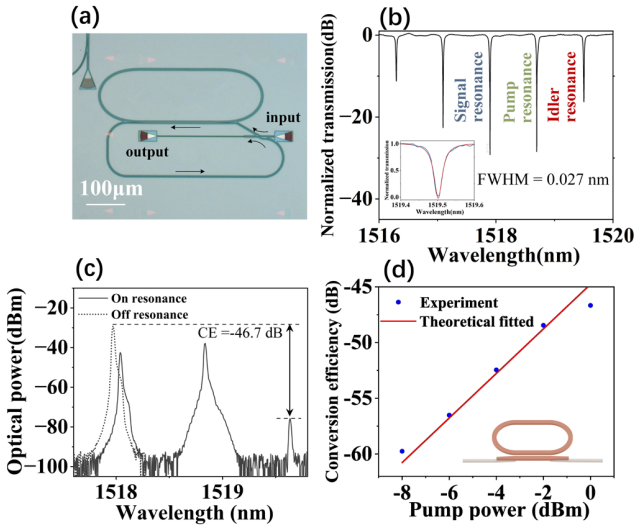

Fig. 4. (a) Microscopic images of the hybrid-integrated MRR. (b) Measured transmission spectrum of the hybrid-integrated MRR (inset: Lorentz fitting for the resonance peak). (c) Measured output spectra of the hybrid-integrated MRR by OSA when the signal is off- and on-resonance. (d) Measured FWM conversion efficiency of the hybrid-integrated MRR as the function of the pump power.

$$L_{eff} = L^2 e^{-\alpha L} \left| \frac{1 - e^{(-\alpha + j\Delta k)L}}{(-\alpha + j\Delta k)\, L} \right|^2, \tag{2}$$

$$F^2 = \frac{P_{ring}}{P_{bus}} = \frac{FSR}{\pi \times FWHM} \times \frac{2Q_l}{Q_c}, \tag{3}$$

where γ denotes the nonlinear coefficient, and P_i, P_s, and P_p represent the optical powers of the idle output, signal, and pump input, respectively. L and L_{eff} represent the round-trip length and effective round-trip length of the micro-ring, while α denotes the propagation loss coefficient within the micro-ring. Δk is defined as the phase mismatch of photons at each frequency in the FWM process, which can be neglected due to the low dispersion and the close proximity of the signal frequency to the pump frequency. $F_{p,s,i}$ respectively indicate the field enhancement factors of the pump, signal, and idle, which are determined by the ratio of optical power within the micro-ring to that in the bus waveguide, as expressed in formula (3). Here, Q_c is the coupled quality factor of the MRR. The L_{eff} was calculated to be $L_{eff} \approx 968\,\mu$m, and the power enhancement factor was $F^2 \approx 30.2$. Furthermore, by fitting the data in Fig. 3(e) using the model described in Eq. (1), we calculated the nonlinear coefficient $\gamma = 11.6\,W^{-1} \cdot m^{-1}$. In conjunction with the mode effective area $A_{eff} = 0.55\,\mu m^2$, we calculated the nonlinear refractive index $n_2 = 1.57 \times 10^{-18}$ m^2/W for $Ge_{28}Sb_{12}Se_{60}$, which is consistent with that of the bulk material and superior to many other materials utilized in nonlinear-integrated photonics.

Through the utilization of the CMOS-compatible MPW process and back-end-of-line techniques, we successfully realized the MRRs featuring the hybrid integration of chalcogenide waveguides and silicon waveguides. The structural diagram of the resonator is presented in Fig. 4(a). The signal and pump input light were coupled into the bottom silicon grating coupler by etching a window through the GSSe layer. The signal and pump

in the silicon waveguide were subsequently coupled to the upper GSSe waveguide via the interlayer coupler and then directed into the MRR. Among them, the interlayer coupling efficiency of the Si-GSSe waveguide can reach up to 98.4% [8]. The signal, pump, and idler coupling to the fiber was achieved through a reverse process that mirrors the input coupling procedure.

Similarly, we first evaluated the hybrid-integrated MRR's performance and analyzed its intracavity propagation loss. Figure 4(b) demonstrates that the hybrid-integrated MRR exhibits a nearly equidistant FSR of approximately 0.81 nm, which corresponds to a calculated group index ng of 2.86. At the same time, by employing Lorentz fitting, the FWHM of the hybrid-integrated MRR was determined to be 0.027 nm. This result corresponds to a calculated loaded quality factor Q_l of 5.6×10^4 and an intrinsic quality factor Q_i of 9.8×10^4, indicating that the propagation loss of the waveguide is approximately 5.23 dB/cm. The lower quality factor of the hybrid-integrated MRR compared to that of the single-layer MRR is analyzed in Supplement 1. Further, we conducted on-chip FWM experiments using the same measurement system described above for the hybrid-integrated MMR. As illustrated in Figs. 4(c) and 4(d), on the Si-GSSe hybrid nonlinear-integrated photonics platform, we also successfully demonstrated the on-chip nondegenerate FWM parametric process with a nonlinear threshold power of less than 0.2 mW (approximately 0.16 mW), and the conversion efficiency of FWM achieved −46.7 dB when the pump power reached 1 mW. Owing to the CMOS-process compatibility of the silicon photonics platform, as well as the high nonlinearity coefficient and excellent manufacturability of chalcogenide glass, this system exhibits a lower nonlinear power threshold and superior robustness in manufacturing compared with hybrid integration platforms such as III/V-silicon and 2D material-silicon waveguides [17,18].

In summary, by leveraging MPW and back-end-of-line fabricated processes, we successfully realized the Si-GSSe hybrid-integrated nonlinear photonics platform and demonstrated the efficient on-chip FWM parametric process. The intrinsic quality factors of the single-layer GSSe MRR and the Si-GSSe hybrid-integrated MRR were measured to be 3.71×10^5 and 9.8×10^4, respectively. We extracted the nonlinear coefficient of the $Ge_{28}Sb_{12}Se_{60}$ material to be approximately $11.6\,W^{-1} \cdot m^{-1}$, and the nonlinear refractive index is about 1.57×10^{-18} m^2/W through the FWM measurement of the single-layer GSSe MRR. Moreover, we have successfully demonstrated the FWM nonlinear parametric process using a hybrid-integrated photonic platform that integrates the GSSe waveguide with the standard MPW silicon photonic wafer for the first time. This achievement features an exceptionally low nonlinear power threshold of 0.16 mW and paves a promising way toward the development of large-scale integrated nonlinear photonics platforms.

Funding. Natural Science Foundation of Zhejiang Province (LD22F040002); the Key Project of Westlake Institute for Optoelectronics (2023GD003/110500Y0022303).

Acknowledgment. The authors would like to acknowledge the fabrication support from the ZJU Nano-Fabrication Center at Zhejiang University, the Westlake Center for Micro/Nano Fabrication and Instrumentation at Westlake University, and the Institute of Microelectronics of the Chinese Academy of Sciences. The authors would also like to thank Xinyu Qiao and Huiling Lu for their assistance with thin-film preparation and characterization.

Disclosures. The authors declare no conflicts of interest.

Data availability. The data that support the findings of this study are available from the corresponding author upon reasonable request.

Supplemental document. See Supplement 1 for supporting content.

REFERENCES

1. M.-G. Suh and K. J. Vahala, Science **359**, 884 (2018).
2. L. Caspani, C. Xiong, B. J. Eggleton, *et al.*, Light Sci. Appl. **6**, e17100 (2017).
3. G. Guan, A. Liu, C. Zheng, *et al.*, J. Light. Technol. **41**, 3208 (2023).
4. V. Pelgrin, H. H. Yoon, E. Cassan, *et al.*, Light Adv. Manuf. **4**, 168 (2023).
5. A. R. Johnson, A. S. Mayer, A. Klenner, *et al.*, Opt. Lett. **40**, 5117 (2015).
6. M. H. P. Pfeiffer, C. Herkommer, J. Liu, *et al.*, Optica **4**, 684 (2017).
7. B. Gholipour, S. R. Elliott, M. J. Müller, *et al.*, J. Phys. Photonics **5**, 012501 (2023).
8. K. Bao, B. Sun, K. Lei, *et al.*, Opt. Mater. **159**, 116622 (2025).
9. L. Wan, J. Huang, M. Wen, *et al.*, Laser Photonics Rev. **19**, 2401832 (2024).
10. C. Wang, J. Song, Z. Ao, *et al.*, Laser Photonics Rev. **18**, 2300893 (2024).
11. J. Song, Y. Peng, X. Guo, *et al.*, Laser Photonics Rev. **18**, 2301128 (2024).
12. M. Wei, K. Xu, B. Tang, *et al.*, Nat. Commun. **15**, 2786 (2024).
13. L. Zhang, L. Jie, M. Zhang, *et al.*, Photonics Res. **8**, 684 (2020).
14. D. Melati, F. Morichetti, A. Melloni, *et al.*, J. Opt. **16**, 055502 (2014).
15. P. P. Absil, J. V. Hryniewicz, B. E. Little, *et al.*, Opt. Lett. **25**, 554 (2000).
16. M. Fu, Y. Zheng, G. Li, *et al.*, Opt. Express **28**, 39084 (2020).
17. G. Marty, S. Combrié, A. De Rossi, *et al.*, APL Photonics **4**, 120801 (2019).
18. M. Ji, H. Cai, L. Deng, *et al.*, Opt. Express **23**, 18679 (2015).